Energy conversion and hydrodynamic analysis of multi-degree-of-freedom wave energy converters integrated into a semi-submersible platform

Yong Cheng[a], Shiqi Dai[a], Saishuai Dai[b,*] , Chunyan Ji[a], Margot Cocard[b], Zhiming Yuan[a, b], Atilla Incecik[b]

[a]*School of naval architecture and ocean engineering, Jiangsu University of Science and Technology, Zhenjiang, 212003, China*

[b]*Naval Architecture, Ocean and Marine Engineering Department, University of Strathclyde, Glasgow, United Kingdom*

ABSTRACT

Keywords:

1. Introduction

Wave energy has rapidly become one of the most promising marine renewable energy because of its predictability and gigantic global power potential that is estimated to reach to available 32,000 KWH per year [1, 2]. In addition, wave energy has much higher intensity estimated about 2–3 kW/m^2 than the intensity of some other types of renewable energy such as 0.4–0.6 kW/m^2 for wind energy and 0.1–0.2 kW/m^2 for solar energy [3], and is available up to 90% of the time compared to 20–30% of solar and wind [4]. Since Stephen Salter came up with the concept of Wave Energy Duck [5] in the 1970s, various wave energy conversion technologies have been proposed based on wave interaction with structures and more than a thousand patents have been issued for wave energy converters (WECs). For example, Oyster WEC [6] and Pelamis WEC [7] in England, WaveRoller WEC [8] in Portugal, IPS buoy WEC [9] in Swedish. However, WECs have not reach the commercial scale deployment yet due to some practical factors, such as high construction cost, low power generation efficiency and single form of motion.

According to the intermediate conversion mechanism of wave energy, the predominant categories of WECs cosist of oscillating buoy device (OBD), oscillating water column (OWC), and overtopping device (OTD) [10]. Nearshore wave energy resources often are considered be less than offshore resources due to energy loss during wave propagation. Thus, earlier WECs are design in axi-symmetric form for deep water in which incident waves are would come from multi-direction and wave energy reserve is assessed based on the omni-directional power. Kim et al. [11] put forward a concentric dual-buoy WEC which consists of external buoy with circular attachment and cylindrical internal buoy in moon-pool, and investigated its hydrodynamic performance under various wave conditions. Kong et al. [12] analyzed numerically and experimentally the power take-off (PTO) optimization scheme of a combined axi-symmetric buoy (CAB) subjected irregular wave loads, revealing that there is an optimal PTO daming for the average energy extraction under each spectral peak period. Subsequently, Guo et al. [13] presented an absorption two-degree-of-freedom (TDOF) WEC with coaxial symmetrical articulated points,

*Corresponding author: Saishuai Dai, mainly research in hydrodynamic performance of marine energy devices
E-mail: saishuai.dai@strath.ac.uk

This is a peer reviewed, accepted author manuscript of the following research article: Cheng Y, Dai S, Dai S, Ji C, Collu M, Yuan Z, Incecik A. 2022. Energy conversion and hydrodynamic analysis of multi-degree-of-freedom wave energy converters integrated into a semi-submersible platform. Energy Conversion and Management. 252:Article 115075. https://doi.org/10.1016/j.enconman.2021.115075

and simulated the energy extraction performance generated by the coupled motions of heave and pitch using a viscous-folw model. Bailey [14] devlepoed a three-dimensional (3D) stochastic model to predict the energy extracted by an array of 50 individual WECs with linear PTO system. Harris et al. [15] reviewed the design principle and adoption of mooring systems for wave energy converters, including the single- to multi-cable, caternary or taut system. Asai and Keita [16] proposed a two-body point absorber consisting of a circular cylinder buoy and a submerged sphere. For this device, a tuned inerter including a PTO system and a tuning spring, is located between these two bodies, and a tuning spring, from which energy can be effectively absorbed by taking advantage of the resonance effect of the inerter part. During recent years, WECs in nearshore region has gradually received attention, as a result of new understanging of the explitable wave energy that is defined as the mean value of the directionally resolved incident wave energy [17]. One type of devices is classified as oscillating wave surge converters (OWSCs). Aquamarine Power Ltd's Oyster is an example of an OWSC which a buoyant flap hinged at seabed-mounted bottom and has the top edge piercing through the water surface [18]. Folley et al. [19] optimized numerically the key design parameters od an OWSC device, such as flap width, resonant frequency, and motion constraints. Cheng et al. [20] developed a fully nonlinear potential flow model to simulate the wave impact effect when the flap enters freely into water surface, showing that a long and thin jet would be generated along the body surface. Another type of nearshore WECs is integrated conventional WEC into a coastal structure. For example, Pereiras et al. [21] described the matched procedure between non-linear turbine PTO and optimal energy transform of an OWC installed in an intended site La Guardia breakwater in northwest coast of Spain. The results indicated that the size of the axial turbine is smaller and rotates at a greater speed than the radial turbine, which leads to a higher mean capture efficiency. Zheng et al. [22] put forward a theoretical model to analyze wave energy absorption of an OWC semi-embedded in a coastal breakwater based on linear potential flow assumption and matched eigen-function expansion method (MEFEM). Heo and Koo [23] calculated the power capture performance of a heaving-buoy WEC connected to a fixed jacket platform and reaction loads between two bodies using the WAMIT software.

The competitiveness of WECs in the energy market can be enhanced by combining two or more marine structures into a single unit due to the increase of energy extraction per-unit area. In addition, the hybrid system of WECs will achieve synergy among multi-purpose objectives by sharing the power infrasturcture. Michailides and Angelides [24] proposed a flexible floating breakwater consisting of multiple WECs installed flexibly between adjacent modules. The relative motion between modules is converted into electric power in the longitudinal and transverse direction by PTO system. Compared to conventional box-type floating breakwater, the power absorbed by oscillating motions with the utilization of PTO can enhance about 10% of wave attenuation capacity. Similar integrated devices include the floating breakwater attached with pile-supported oscillating water column (OWC) [25], overtopping device (OTD) [26] and oscillating buoy device (OBD) [27]. Liu et al. [28] proposed a semi-submersible fish cage-WEC integrated platform, providing a more economical and effective method for the offshore aquaculture. To realize cost-sharing, Muliawan et al. [29] considered a combined concept consisting of a spar-type floating wind turbine (FWT) and an axisymmetric two-body WEC. Preliminary numerical studies indicated that the proposed combined concept increases the total power extraction compared that for an isolated FWT and WEC concept. Based on this design

concept, Ren et al. [30] proposed a heaving WEC installed on a fixed monopole-type wind turbinbe, and conducted the corresponding numerical and experimental tests which revealed the synergies between wave and wind energy exploitation. The efficiency of array WECs integrated into a FWT platform was further studied by Hu et al. [31]. Even though the nonlinear factors are neglected in the linear potential model, conclusions derived from numerical results verified the reduction fo horizontal loads on the floating platform due to addition of WECs. The integrated large floating platform between wave energy converters and other marine structures is very popular among the extensive studies. Fiaschi et al. [32] put forward a new offshore platform, which is used as the compressed air energy storage (CAES) system integrated with three energy storage systems. Zhang et al. [33] investigated the relationship between energy extraction and platform stability for a hydraulic PTO embedded in the modularized floating platform by hinge connectors. To obtain a broader range of wave heights and wave frequencies, Sricharan and Chandrasekaran [34] designed three bean-shape platform configurations combing a central cylindric floater and some heaving WECs around it. Furthermore, the integration brings some benefits which include: (i) increasing WECs reliability because other purpose marine structures can provide additional strength to WECs to operate in strong wave conditions; (ii) reducing mooring/foundation footprints; (iii) increasing the efficiency in using ocean space because the ocean space is used for multiple purposes limiting negative environmental effects. Above-mentioned works have improved effectively the power extraction performance by integrating WECs with marine platforms, but are limited to single-degree-of-freedom (SDOF) motion of WECs, which will be only appropriate for given range of water depth i.e. nearshore or offshore. Therefore, the motivation of this paper is to develop a WEC integrated system with multi-degree-of-freedom (MDOF) motion, which can capture both omni-direction and uni-direction wave energy resoures.

Advanced theoretical and numerical techniques have been widely used for simulating the power performance of the integrated WEC system. Based linear potential flow theory, Zhao et al. [35] developed an analytical model to investigate the hydrodynamic performance of heaving WECs embedded in a comb-type breakwater. It is found that the maximum capture efficiency of the integrated system can achieve 70% due to wave resonance in chambers. Sun et al. [36] employed a boundary element method (BEM) to investigate wave energy capturing capacity of a novel floating array-buoys WEC system and validated numerical soultions by comparing with experimental results. Ren et al. [37] coupled the hydrodynamic and aerodynamic models to illustrate the mechanical and hydrodynamic interactions between a tension leg platform type FWT and a heaving WEC. Zhong and Yeung [38] adopted an efficient semi-anlutical method by matching eigen-function expansins for inner and outer domains, to simulate wave interaction with multi-truncated cylindrical WEC integrated system. Along the same lines, Zheng et al. [39] investigated power capture performance of a hybrid system combing OWC and OB-type WECs, showing that because of a destructive array effect, the hybrid WEC system is advantageous for wave energy extraction compared with single-type WEC system. Zhou et al. [40] presented a 3D time-domain model to reveal the coupled hydrodynamic response of an OWC WEC integrated into a monopole-mounted offshore wind turbine. In their simulation, the surface elevation and air pressure inside the chamber were predicted and comparied with measured data. Some viscous-flow models based on computational fluid dynamics (CFD) were also established to accurately calculate the viscous losses and vortex shelding induced by integrated WEC systems.

Reabroy et al. [41] developed a 2D CFD wave flume using Star-CCM+ software to study the hydrodynamic performance of an asymmetric OB-type WEC installed in front of a cylindric fixed breakwater, showing clearly vorticity shade around the smooth line of the WEC model. As a general extension, Zhang et al. [42] analyzed systematically the effects of asymmetrical features of WEC device on wave energy extraction, and found that compared the conventional symmetrical WEC device, the asymmetrical wedge-shaped body has a beneficial effect on capture efficiency due to reduction of transmitted wave energy at the leeside of integrated system. Windt et al. [43] developed a CFD model based on numerical wave tank using an OpenFOAM library to validate the effective energy absorption of a point-absorber WEC device installed at a fixed platform. Marchesi et al. [44] conducted CFD numerical simulations to estimate the energy absorption of a two-degree-of-freedom (TDOF) system composed of a heaving floater and a surging paddle under regular and random wave conditions.

Previous existing WEC integrated systems are developed with different design concepts and energy extraction principles. However, the relating works on the WEC system with multi-degree-of-freedom (MDOF) are still scarce compared with the studies on SDOF WEC system. Moreover, it is not possible to infer the effect of multi-body interaction on the energy extraction performance from published studies. The novelty of this work is twofold; firstly to present a MDOF-WEC system integrated in a semi-submersible platform as the basic model which is suitable for both deepwater region and coastal region, and secondly to obtain a comprehensive understanding of the mutual relatiship among different type WECs and platform through a series of parametric analysis, aiming at the problem of low power capture efficiency. This will help to space-sharing, cable-sharing and manpower-sharing WEC integrated system solutions that help to reduce the overall cost of wave energy extraction.

This paper is arranged as follows. In Section 2, the details of the novel MDOF-WEC integrated system is introduced according the configuration principles. Section 3 presents the CFD numerical model in a 3D wave tank based on viscous-flow theory with Navier-Stokes equations. Then the convergence and validation of the numerical solutions are given in Section 4. In Section 5, the comparisons of the hydrodynamic performance among the hybrid system combing MDOF WECs and a semi-submersible platform and the isolated WECs are given. The effects of the structural dimensions, the water depth and the wave steepness on WEC motion response, energy extraction, wave forces on platform and wave elevation are discussed. Finally, the conclusion is presented in Section 5.

2. Configuration of WECs and platform

2.1 MDOF-WEC system

Fig. 1(a) shows the MDOF-WEC system which consists of a dual-cylindrical oscillating wave surge converter (OWSC) and two oscillating buoys (OBs). The dual-cylindrical oscillating wave surge converter which is hinged at the bottom of the platform, oscillates back and forth under the wave action. Two identical OB-type WECs are restrained on each cylinder, respectively. Some slide rails are used to connect OWSC and OB. From previous studies [12, 41, 42 and 43], it is found that compared with the convetional OB with flat bottom, the OB with spherical bottom has higher wave energy absorption due to less vorticity loss. Thus, each OB is divided into two parts: the upper cylinder and the lower hemispherical bottom with same radius R. The working principle of the MDOF-WEC system is described as shown in Fig. 1(c). The pitch motion of the

dual-cylindrical OWSC together with two OBs drives directly the PTO system which is linked between WEC and platform, and wave energy is converted into electricity. On the other hand, motions of each OB along cylinder surface are controlled by a PTO system installed above the OWSC device, and some wave energy can be extracted in the form of the kinetic energy of relative motion between OB and OWSC. The geometric parameters including radius cylinder, radius of OB and draft of OB has an importance influence on the performance of of the MDOF-WEC system, and systematically examined in this paper.

2.2 Semi-submersible platform

The semi-submersible platform is composed of six columns at corners in which upper and lower three columns are distributed in equilateral triangle shape with same dimensions, respectively. Some trusses are located at between columns, which reduce the disturbance on wave energy capture due to the presence of platform and provide open water for the MDOF-WEC system. In addition, the trusses among upper columns are design to be simple curved structures which create a larger topside space. In order to reduce the motion response of the platform, one damping plate directly installed at the bottom of each lower column are expected to generate viscous damping and more added fluid mass. Fig. 1(b) shows the configuration of the semi-submersible platform, and detailed dimensions are summarized in Table 1.

Table 1 Detailed information of MDOF-WEC system and integrated platform

Configuration	Item	Symbol	Value	Unit
OWSC device	Radius	R_c	0.975	m
	Height	H_c	10.5	m
	Draft	d_c	7.5	m
	PTO damping	$b_{\text{pto(OWSC)}}$	6.86×10^5	N•m•s/radian
OB device	Inner radius	R_{oi}	1.16	m
	Outer radius	R_{oo}	2.1	m
	Height	H_o	3.3	m
	Draft	d_o	1.8	m
	PTO damping	$b_{\text{pto(OB)}}$	7.00×10^3	N •s/m
Platform	Column radius	R_p	2.025	m
	Column height	H_p	2.1	m
	Column-column distance	h_c	6.3	m
	Damping plate radius	R_d	2.475	m
	Damping plate height	H_d	0.3	m

2.3 Design characteristics

There are existing some works which improve wave energy capture efficiency by integrating WECs with marine platforms. These WEC-platform integrated systems are mainly focus on fixed ocean environment and are designed to extract wave energy by converting SDOF motion of WECs. Comparatively, the novel MDOF-WEC integrated system proposed in this paper has the following characteristics: (1) This integrated system has higher capacity of wave energy extraction by combing the advantages of OWSC and OB devices; (2) The application of this integrated system is not restricted by water depth and is suitable for both deepwater and shallow water, i.e. OWSC for extracting horizontal motion of water particles in shallow water and OB for extracting heaving

motion of water particles in deepwater; (3) The MDOF-WEC system can be installed at platform bottom by a self-steering device, and thus the MDOF-WEC system can rotate freely inner platform and automatically heading toward incident waves; (4) An array layout of this integrated system can be quickly arranged to meet the different electricity requirements due to the modular and unitized construction; (5) Some monitoring instruments can be located inside columns to obtain wave condition and environmental data in time and then thse data can be compressed in a database to be transfer to onshore acquisition center.

3. Mathematical model

In this paper, a 3D numerical tank is established to model the interaction of waves with the MDOF-WEC system integrated into a semi-submersible platform, as shown in Fig. 2. The whole numerical tank is divided into three zone: wave-making zone, working zone and wave-absoring zone. the The semi-submersible platform simulated as six columns with same radius R_p and height H_p, is laied in the working zone and is asuumed to be fixed because its motion is small enough compared to the WEC system. The MDOF-WEC system combing a dual-cylindrical OWSC and two OBs, is installed at the bottom of the platform. The radius, height and draft of the OWSC are denoted by R_c, H_c, d_c, respectively. The geometrical parameters of the OB includes inner radius R_{oi}, outer radius R_{oo}, height H_o and draft d_o. The gap between OWSC and OB is set as l_g. The static water depth is defined as h_w. The OWSC device oscillates back and forth along incident waves, and two OBs moves along the body surface of the OWSC device.

3.1 Flow field model

The realizable k-ε turbulence model has been succefully adopted in many wave interaction with marine structures [45-47], and is an adaptable substitue for flow field involving strong multi-body hydrodynamics. For waves interaction with the WEC-platform integrated system, strong wave distaurbance exist due to the coupling effect between WECs. Therefore, the realizable k-ε turbulence model is selected to solve this energy extraction problem, and the corresponding governing equations are mass continuity equation:

$$\frac{\partial \rho}{\partial t}+\frac{\partial \rho u_i}{\partial x_i}=0 \tag{1}$$

and momentum equation:

$$\frac{\partial u_i}{\partial t}+u_j\frac{\partial u_i}{\partial x_j}=-\frac{1}{\rho}\frac{\partial p}{\partial x_i}+g_i+\frac{(\mu+\mu_t)}{\rho}\frac{\partial}{\partial x_j}\left(\frac{\partial u_i}{\partial x_j}\right) \tag{2}$$

where t is time; μ and ρ are the viscosity and density of the fluid, respectively; i, j=1,2 and 3 denoting (x, y, z); u_i and g_i are the velocity and acceleration component, respectively; μ_t represents the eddy viscosity; the third term on the right-hand side of Eq. (2) denotes the viscous part of the stress tensor; $P=p+(2/3)\rho c$, where p is pressure; c is the turbulent kinetic energy. A volume of fluid (VOF) method is used to capture the free surface elevation in the two-phase flow model, and the volume fraction α is described as $\alpha=V_w/V_t$, where V_w and V_t denote the water volume and the total volume in a cell, respectively.

The turbulence kinetica energy equation and ε equation in the realizable k-ε turbulence model are expressed as

k equation:

$$\frac{\partial(\rho c)}{\partial t}+\frac{\partial(\rho c u_i)}{\partial x_i}=\frac{\partial}{\partial x_j}\left[\left(\mu+\frac{\mu_t}{\sigma_c}\right)\frac{\partial c}{\partial x_j}\right]+G_k-\rho\varepsilon \tag{3}$$

ε equation:

$$\frac{\partial(\rho\varepsilon u_i)}{\partial x_i}+\frac{\partial(\rho\varepsilon)}{\partial t}=\frac{\partial}{\partial x_j}\left[\left(\mu+\frac{\mu_t}{\sigma_\varepsilon}\right)\frac{\partial \varepsilon}{\partial x_j}\right]+\rho C_1 S\varepsilon-\rho C_2\frac{\varepsilon^2}{k+\sqrt{\nu\varepsilon}}+C_{1\varepsilon}\frac{\varepsilon}{k}C_{3\varepsilon}G_b \tag{4}$$

$$C_1=\max\left[0.43,\frac{\kappa}{\kappa+5}\right],\quad \kappa=S\frac{c}{\varepsilon},\quad S=\sqrt{2S_{ij}S_{ij}}\,,\ S_{ij}=\frac{1}{2}\left(\frac{\partial u_i}{\partial x_j}+\frac{\partial u_j}{\partial x_i}\right) \tag{5}$$

where S is the modulus of the mean rate-of-strain tensor; G_k denotes the turbulent kinetic energy generated by the average velocity gradient; C_2=1.9 and $C_{1\varepsilon}$ =1.44 are constants; σ_c=1.0 and σ_ε=1.2 denote turbulent Prandtl number.

The corresponding boundary conditions in the numerical 3D wave tank is set as follows. The left boundary is specified as the velocity inlet boundary condition which generates directly the fifth-order incident waves [48], while the right boundary is defined as outflow boundary condition. The tank lateral surfaces and the bottom surface are modelled as the wall boundary condition with zero shear loads. On the tank top, the pressure outlet boundary condition is implemented to match with the atmospheric pressure. A forcing method [42] is employed in both wave-making zone and the wave-absoring zone to eliminate gradually the reflecting waves from the the WEC-platform integrated system.

3.2 Motion and energy extracion of MDOF-WEC system

The MDOF-WEC system comprises a dual-cylindrical OWSC and two OBs, and its motion responses can be expressed as

Motion of OWSC:

$$I_{(OWSC)}\ddot{\gamma}+b_{pto(OWSC)}\dot{\gamma}+c_{pto(OWSC)}\gamma=M_{f(OWSC)} \tag{6}$$

Motion of each OB:

$$m_{(OB)}\ddot{x}_i+b_{pto(OBx)}\dot{x}_i+c_{pto(OBx)}x_i=F_{fxi(OB)} \tag{7}$$

$$m_{(OB)}\ddot{z}_i+b_{pto(OBz)}\dot{z}_i+c_{pto(OBz)}z_i=F_{fzi(OB)}-mg \tag{8}$$

where $I_{(\mathrm{OWSC})}$ denote the rotational inertia of the OWSC; $m_{(\mathrm{OB})}$ denote the mass of each OB; γ, $\dot{\gamma}$ and $\ddot{\gamma}$ are rotational displacement, rotational velocity and rotational acceleration of the OWSC device, respectively; γ is zero when the initial position of the OWSC is identical with the vertical direction; x_i and z_i the horizontal and vertical component of motion response for i-th OB; $M_{f(\mathrm{OWSC})}$ is the force moment on OWSC due to waves as well as gravity; $F_{fxi(\mathrm{OB})}$ and $F_{fzi(\mathrm{OB})}$ are the horizontal and vertical wave forces on i-th OB, respectively; g is the acceleration due to gravity; b_{pto} and c_{pto} are the PTO damping cofficient and stiffness coefficient, respectively. Because two OBs are respectively installed on each cylinder of the OWSC, OBs move together with the rotation of OWSC and the motion relationship between OWSC and OB can be written as

$$z_i=x_i\tan\gamma \tag{9}$$

The motion displacement s_i of each OB along the body surface of the OWSC can be calculated

as

$$s_i = z_i \cos\gamma \tag{10}$$

Based the equilibrium principle of the inertial term and the restoring force [16], the natural periods $T_{n(\mathrm{OWSC})}$ for OWSC and $T_{ni(\mathrm{OB})}$ for i-th OB can be written as

$$T_{n(OWSC)} = 2\pi / \sqrt{\frac{(c_{pto(OWSC)} + c_{z(OWSC)})}{I_{(OWSC)} + a_{z(OWSC)}}} \tag{11}$$

$$T_{ni(OB)} = 2\pi / \sqrt{\frac{(c_{pto(OB)} + c_{zi(OB)})}{m_{(OB)} + a_{zi(OB)}}} \tag{12}$$

where $a_{z(\mathrm{OWSC})}$ and $a_{zi(\mathrm{OWSC})}$ are the added mass which can be obatiend through linear potential model [49, 50] for OWSC and i-th OB, respectively. $c_{z(\mathrm{OWSC})}$ and $c_{zi(\mathrm{OB})}$ are the restoring force coefficients due to the difference between the hydrostatic term and the structural weight.

For the WEC integrated system with MDOF motions, the optimal PTO damping coeffiecient $b_{\mathrm{opt(OWSC)}}$ for the OWSC and $b_{\mathrm{opti(OB)}}$ for i-th OB can calculated, respectively [16, 42]

$$b_{opt(OWSC)} = \sqrt{\frac{((I_{(OWSC)} + a_{z(OWSC)})\omega^2 - (c_{pto} + c_{z(OWSC)}))^2}{\omega^2}} + b_{z(OWSC)} \tag{13}$$

$$b_{opti(OB)} = \sqrt{\frac{((m_{(OB)} + a_{zi(OB)})\omega^2 - (c_{pto(OB)} + c_{zi(OB)}))^2}{\omega^2}} + b_{zi(OB)} \tag{14}$$

where $b_{z(\mathrm{OWSC})}$ and $b_{zi(\mathrm{OB})}$ are radiation damping for OWSC and i-th OB, respectively. ω is incident wave frequency.

The rotational motion of the OWSC device and the translational displaments along the OWSC surface of two OBs are converted into electricity by PTO system, and the total average generated power E_p includes the $E_{p(\mathrm{OWSC})}$ for OWSC and $E_{pi(\mathrm{OB})}$ i-th OB for as follows

$$E_p = E_{p(OWSC)} + \sum_{i=1}^{2} E_{pi(OB)} \tag{15}$$

$$E_{p(OWSC)} = \frac{b_{pto(OWSC)}}{nT} \int_{t}^{t+nT} \dot{\gamma}^2 dt \tag{16}$$

$$E_{pi(OB)} = \frac{b_{pto(OB)}}{nT} \int_{t}^{t+nT} \dot{s}_i^{\,2} dt \tag{17}$$

where n is the number of WEC motion period; T is incident wave period.

The capture efficiency R is an important factor to evaluate the wave energy conversion, and can be expressed as [42]

$$R = \frac{E_p}{E_w} \tag{18}$$

where incident wave energy E_w within one incident wave period can be obtained from [41]

$$E_w = \frac{1}{8}\frac{\rho g H_I^2 \lambda R_o}{T}\left(1+\frac{2(2\pi/\lambda)h}{\sin\left[2(2\pi/\lambda)h\right]}\right) \tag{19}$$

where λ is the wavelength, and H_I is incident wave height.

To discern the influence degree of the hydrodynamic interaction between the platform and the WEC system on wave motion, the wave coefficient C_w is defined as follows

$$C_w = \frac{\eta_{\max} - \eta_{\min}}{H_I} \tag{20}$$

where $\eta_{\max}$ and $\eta_{\min}$ denote the maximum and minimum wave elevation, respectively.

3.3 Numerical solution

A 3D numerical wave tank in which the WEC-platform integrated system is located, is divided into a finite number of control volumes using Star-CCM+ CFD software. In this model, the govering euqations are discretized using finite volume method (FVM) package [51], and are solved using a second order pressure-based solver with implicit and unsteady formulations [52] to achieve converged results. The discretization scheme for pressure, momentum, turbulent kinetic energy and turbulent dissipation rate are carried out using a quadratic upwind interpolation of convective kinematics algorithm. All simulations are defined as having reached the converged results when all the residuals are reduced to less than 0.001.

3.4 Grid generation scheme

A series of hexahedral grids in the whole numerical tank are automatically generated by using the Star-CCM+ Grid Generation. In order to retain a high grid quality when the floating bodies move at every time step, a trimmed grider is used to generate meshes of the encryption region near free and body surfaces and the transition region from fluid to structure. In addition, a prism layer grider is selected to create some prismatic layers i.e. ten layers in this paper around the structure, which avoids the excessive distortion of the grids and ensures the continuous matching conditions of the fluid pressure and velocity.

Some overset multi-block chimera grid zones as shown in Fig. 3, are generated by using a trimmed mesher solver to simulate the MDOF motions including pitch, sway and heave of the combined WEC system. These overset zones include two motion zones of the OB device, a motion zone of OWSC device, six columnar zones of platform and whole numerical tank zone, in which the grid shape is not affected by the body motions and thus the grids around the body retains a good quality. The coupling effect of overset zones is interpolated based on the dynamic distinction of different grid types i.e. motion grid, fixed grid and interpolated grid. Due to no necessary to remesh the comuplational domain and the accuracy improvement of grid motion with large amplitude, the overset grid scheme has been successfully applied for many wave-structure interactions [54].

4. Experiments complementary to numerical performances

In order to validate the numerical procedure and the design feasibility described in the previous sections, a seris of experiments were also carried out in 3D wave tank (long 38 m, 15 m wide and 1.2 m deep) located at University of Jiangsu Science and Technology (JUST). The tank is equipped with a piston type wave maker at one end to produce incident waves and an artificial damping beach at another end and absorb transmitted waves. The physical MDOF-WEC model

was constructed with a 1:15 scale of the designed protype shown in Table 1. Fig. 4 displays the assembly process of each component and the final model configuration. The OB-type and OWSC-type WECs were made of 20-mm thick acrylic sheet and 10-mm thick aluminimum sheet, respectively. The OB device moves along the OWSC surface by two pulleys installed in the slide rail with friction coefficienct of 0.03, and the corresponding PTO system was modeled by a permanent magnet linear generator (PMLG) installed inside of the OWSC which can generate electrical power by the rotation of the bevel gear as shown in Fig. 5(a). The PTO system for the OWSC device was also adopted by a PMLG installed at the top of the platform to avoid the possible permeability of water. The rotational motion of the OWSC directly drive the axially fixed gear and then is converted into the heaving motion of a toothed rack acting on the PMLG. The damping force of each PTO system is adjusted by a resistor whose voltage is equal to the electrodynamic potential of the generator. The platform model was composed of six columns, upper deck and connected trusses which were made of 15-mm thick acrylic sheet, 10-mm thick aluminimum sheet and 2-mm thick stainless steel pipe, and fixed at the the middle location of the wave with constant water depth h_w=1.0 m. A light bulb with specific resistance value is located at the top of the platform to illustrate the effect of the power generation, as shown in Fig. 6. A non-contact optical Qualysis tracking system with a maximum error of 0.001 mm is used to obtain the motion displacements of the OB and OWSC devices.

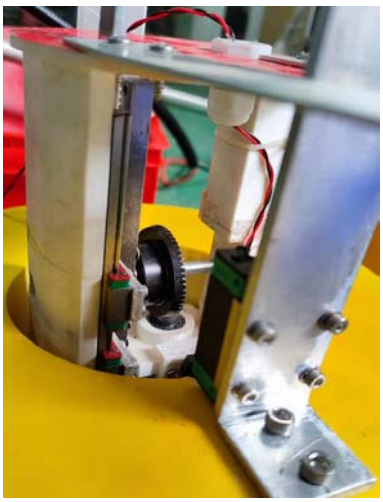

4. Convergence study and comparison

4.1 Convergence study

A MDOF-WEC system integrated into a semi-submersible platform, regard as a representative model of the present work, is chosen to conduct the mesh and time convergent studies. The model dimensions of the numerical example are same with the experimental model described in Section 4. The whole numerical tank is established as 8λ(length) ×1.5 m (width) ×1.5h_w (height), where the length of the wave-absoring zone is defined as 1.5λ. Three different mesh divisions are examined. For example, Mesh a defined the basic element size as $\Delta x=\Delta y=H_I/10$ and $\Delta z=H_I/20$ in encryption zone of water surface. In the transition zone from water surface to tank bottom or top, element size is $\Delta x=\Delta y=H_I/4$ and $\Delta z=H_I/10$. In overset zones, the element size is set as 1/30 times the smallest structural size. Mesh b is the coarser mesh scheme, where the element number is 1/2 of that of Mesh a in encryption and overset zones. Mesh c is the finer mesh scheme, where the element number is doubled compared to Mesh a in encryption and overset zones. Fig. 4 shows the pitch velocity of the OWSC device, the surge and heave velocities of the i-th OB device with different meshes for the incident wave height H_I=0.05 m and incident wave period 1.0 s. In this case, the time step is given as d$t=T/1000$. The PTO damping coefficient for the OWSC device and each OB device are set as $b_{\text{pto(OWSC)}}$=3.5 N•m•s/radian and $b_{\text{pto(OB)}}$=8 N•s/m. Due to the symmetry of both the fluid field and the configuration, two floaters are simulated to oscillate at unison. Thus, showing the performance of only one floater is sufficient to

characterise the performance of the whole floater system. It can be observed that there exists a phase difference which is larger than 5% between Mesh a and Mesh b although the amplitude difference is smaller than 5%. Mesh a correlates well with Mesh c with only slight phase and amplitude differences of both less than 5%. Furthermore, the temporal convergent simulations are conducted with three-time steps: $dt=T/500$, $dt=T/1000$, and $dt=T/2000$, as shown in Fig. 5. All results converge very rapid with decreasing time step, and only slight difference between $dt=T/1000$ and $dt=T/2000$, less than 5% in crests and troughs. Therefore, Mesh a and time step $dt=T/1000$ are used in the following cases.

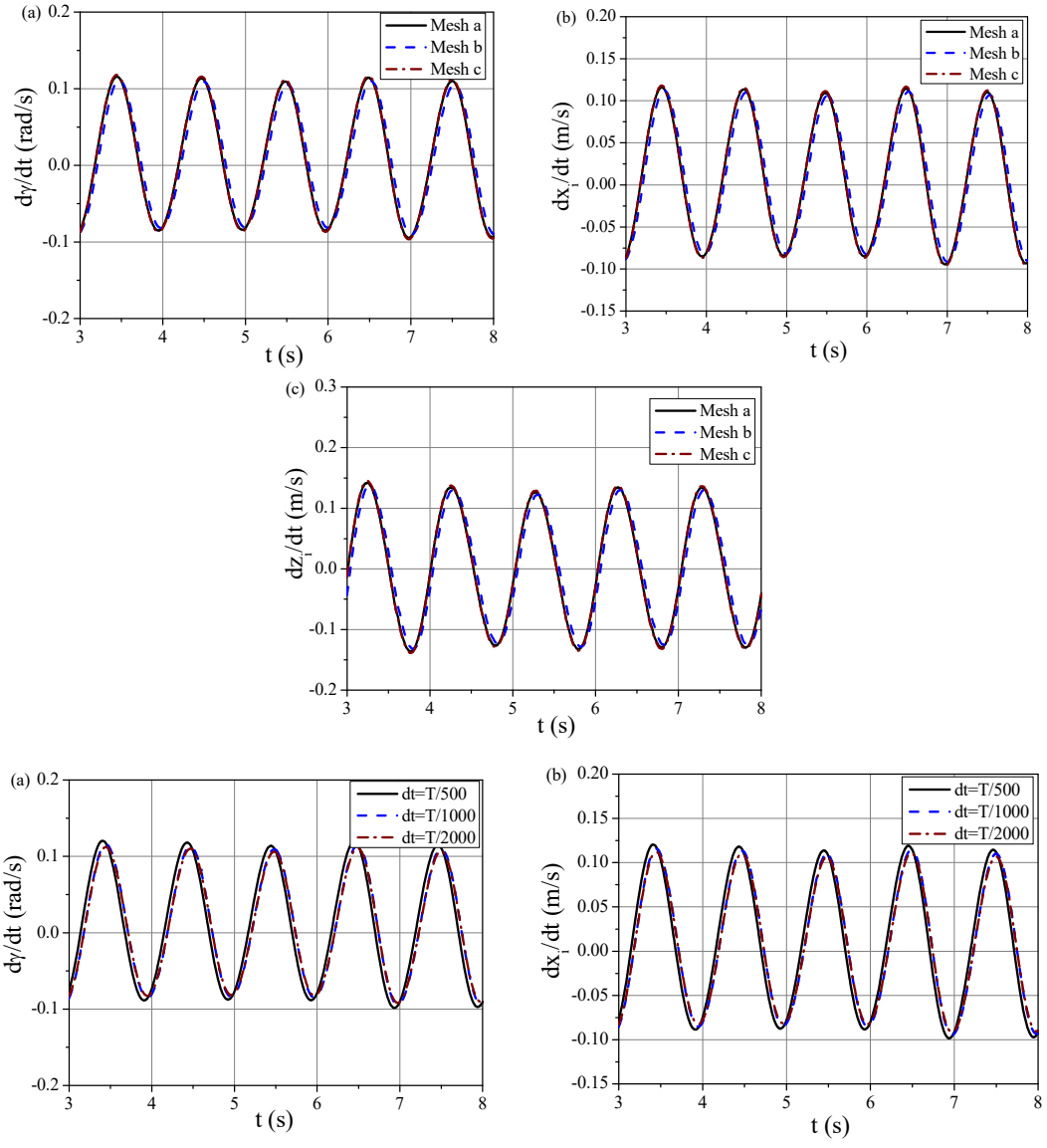

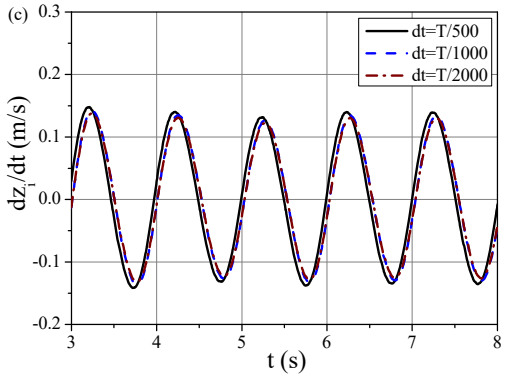

4.2 Comparison with published results

To verify the accuracy of the present CFD simulations, the scale 1:50 experiment of a hybrid system combing a fixed monopile-type wind turbine and a heaving WEC as shown Fig. 6 by Ren et al. [30] is considered, with monopile radiaus R_c=0.12 m, monopile height H_c=1.8 m, WEC outer radius R_{oo}=0.16 m, inner radius R_{oi}=0.08 m, WEC draft d_o=0.06 m. The constant water depth is H_w=0.3 m. Table 2 give the tested conditions for the hybrid system, including the PTO damping loads F_{pto}, corresponding wave heights and wave periods. In order to easily compare with the published results, the numerical results are translated in protype data according to Froude law of similarity. Fig. 7 gives the variation of the average generated power E_p and the heaving amplitude of the WEC device with wave period. The linear potential flow solutions given by Ren et al. [30] is also presented. It can be observed that the linear potential solutions over-estimate obviously the wave energy extraction i.e. the maximum error about 15% for E_p since it igonres the viscous dissipation and the motion nonlinearity, but the occurring condition of the maxium E_p by the potential flow solutions and the present CFD solutions agree well with each other. Moreover, the variation trend of the energy and response curves is almost identical between two numerical methods. Overall, the present model is better agreement with the tested data than the linear potential flow solutions of Ren et al. [30], especially for the wave energy extraction which is over-estimated about 7% at resonant period. The former consider adequately the contribution of the viscous damping and vortex shedding to hydrodynamics, and is sufficiently accuracy for simulating the hydrodynamic performance of the hybrid system in this paper.

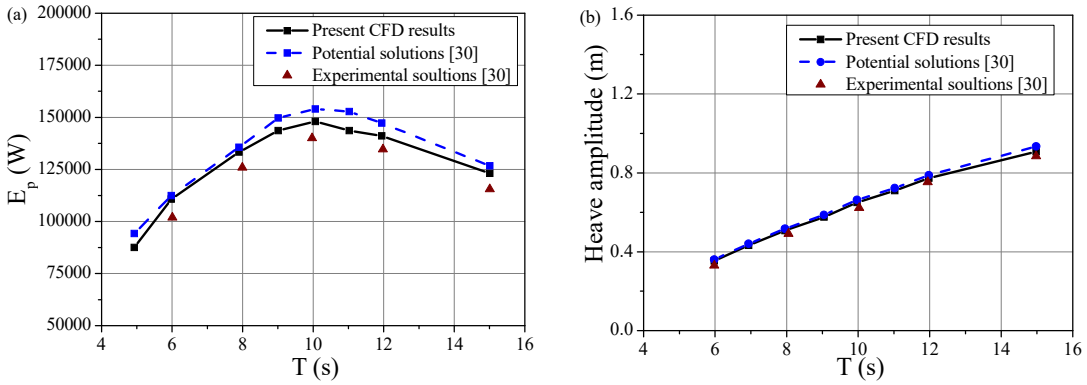

4.3 Comparison with experimental measurements

The numerical results are then compared with the experimental data obtained from Section 3.

In these cases, the incident wave height is fixed as H_I=0.05, and the wave period ranges from T=1.4 s to 2.0 s. The numerical PTO damping coefficient for the OWSC device and each OB device are determined as $b_{pto(OWSC)}$=3.5 N•m•s/radian and $b_{pto(OB)}$=8 N• s/m, to ensure that they generate the same PTO loads with those in the experiment. Fig. 8 gives the time series of the heaving motion of the OB and the rolling motion of the OWSC for T=1.8 s. It can be seen that numerical solutions agree well with experiment results among magnitude, period and phase. Furthermore, the data over a time interval of seven wave periods (t=5T-12T) is adopted for averaging. These averaged peak values and the total power capture efficiency R at each wave period are summarized in Table 3. Here, the terms "CAL." and "EXP." denote the calculated and experimental results, respectively. It can be found from table that the numerical simulation slightly overestimate the motion magnitudes and the capture efficiency of WECs. This may be due to the frictions between the OB and the vertical pile, leading to the extra damping loads.

Generally, the level of agreement with the model tests is rather satisfactory, indicating that the presented multi-body CFD model can accurately predict the hydrodynamic performance of the MDOF-WEC integrated system, and thus allowing an exploration of parametric studies systematacially and supporting supplementary understanding to experimental data.

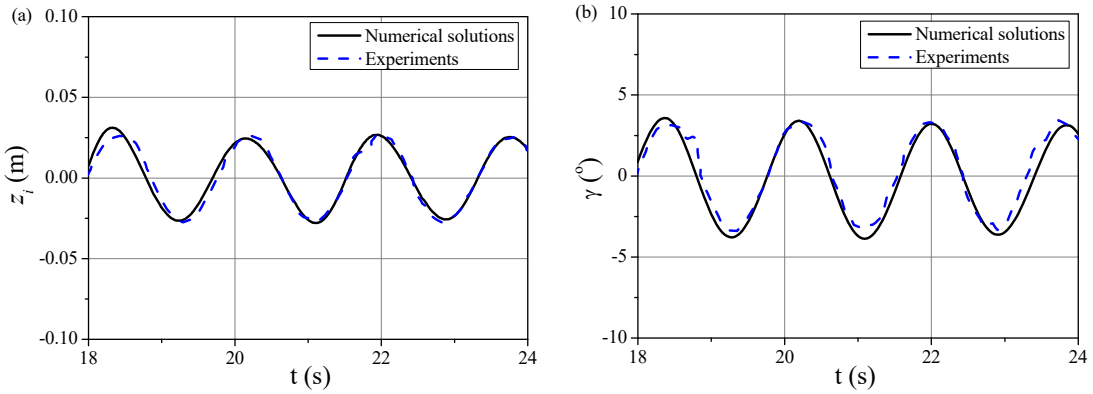

T (s)	H_I (m)	*CAL.* s_i (m)	*EXP.* s_i (m)	*CAL.* γ (deg)	*EXP.* γ (deg)	CAL. total R	EXP. total R
1.4	0.05	0.029	0.027	2.125	2.115	0.182	0.139
1.6		0.032	0.030	2.583	2.553	0.123	0.091
1.8		0.037	0.035	3.131	3.033	0.081	0.071
2.0		0.045	0.044	4.477	4.435	0.075	0.061

4. Numerical results

Based on the verified numerical scheme, the comparsion among the present MDOF-WEC system, the isolated OWSC WEC and the isolated dual-OB WEC is firstly peformed in this section. And then, the influences of the incident wave amplitude, the PTO mechanical coefficient and the WEC geometric variables on the motion response, average generated power and energy capture efficiency as well as water surface elevation are studied. The main objective is to guide the design of an optimum MDOF-WEC integrated system with high wave energy extraction.

4.1 Comparison with typical isolated SDOF-WEC devices

To illustrate the interactions among the OWSC device, the OB device and the platform, three different concepts are considered, i.e. the present MDOF-WEC integrated system, a stand-alone OWSC WEC and a stand-alone dual-OB WEC. The main geometric parameters and the water depth are given in Section 3.1. Fig. 9 shows the variations of the response amplitude operator (RAO) of the OB translation and the OWSC rotation against dimensionless wave period $T(g/H_I)^{1/2}$ for three designed concepts. It can be seen from Fig. 9(a) that the OB motion of the MDOF-WEC device is larger than the isolated OB motion, especially in long-period waves. The can be explained by the motion mode in two-degree-of-freedom. The OB motion of the MDOF-WEC device includes heaving and surging modes while the isolated OB only has heaving motion mode. When long-period waves interact with the OB WEC, the OB moves in phase with the surface waves, amplifying the motion amplitude of the OB. Fig. 9(b) indicated that in short-period waves (about $T(g/H_I)^{1/2}<4$), the rotational displacement of the MDOF-WEC device is larger than that of a stand-alone OWSC WEC, but this follows completely an opposite variarion in $4<T(g/H_I)^{1/2}<5$. It is interesting that when $T(g/H_I)^{1/2}>5$, the motion amplitude of the stand-alone OWSC tends to toward same, while that of the MDOF-WEC device further increase with wave period. This can be acctributed to the fact that the rotational motion of the OWSC is proportional to both the moment arm and the external force. The moment arm induced by the contact force between the OB and the OWSC is found to increase with wave period due to amplified motion of the OB as shown in Fig. 9(a), and thus the rotational motion of the MDOF-WEC device may increase. On the other hand, the contact force generated by the OB device would suddenly increase with the OWSC motion, which in turn enhance the rotational motion of the OWSC.

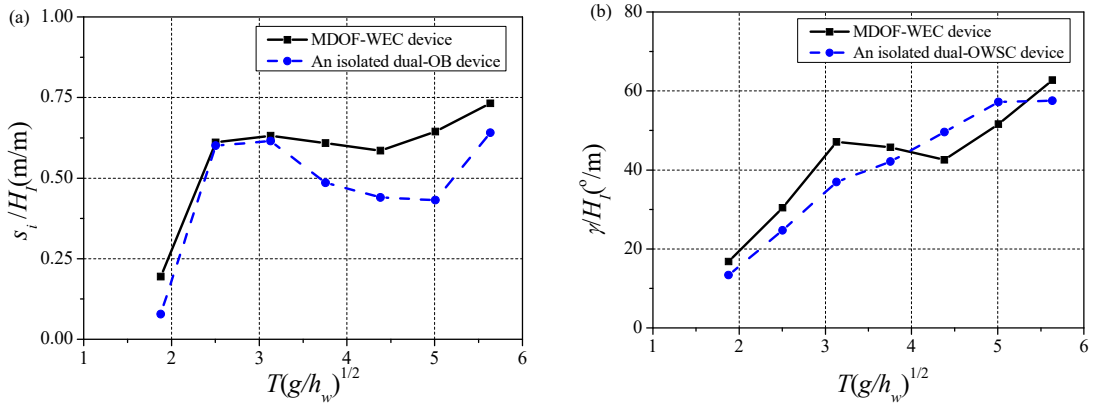

Fig. 11 shows the comparison of the dimensionless average generated power $E_p/(\rho r^{3/2}h^{7/2})$ and the capture efficiency R among three design concepts. It can be observed that the wave energy extraction of the OB device installed at the MDOF-WEC system is substantially higher than that of the isolated dual-OB device, with a maximum increase ratio of 25.7% for the capture efficiency near resonant period $T(g/H_I)^{1/2}=2.5$. This is because the presence of the OWSC enhances the oscillating performance of the OB at the resonant period. The wave energy extraction of the OWSC installed at the MDOF-WEC system is reduced compared with the isolated OWSC device, and hence the OWSC device does not have the benefit from the integrated system. However, the total wave energy extraction of the MDOF-WEC system is greatly improved compared with the isolated WEC devices in whole simulated wave region, with an average increased efficiency ratio of 60.05% for the OB device and 93.15% for the OWSC device, which broadens the effecitive

frequency bandwith of surrounding practical wave farm. The maximum energy extraction of the OB and the OWSC occur at different wave periods, namely, $T(g/H_I)^{1/2}$=2.5 and 3.1, respectively. The occurring period of the maximum efficiency of the MDOF-WEC system is mainly dominated by the OB. The coexistence of these different resonant periods causes higher wave energy extraction and flatter effective frequency bandwith of the MDOF-WEC system. The It is also notable that the maximum capture efficiency of the MDOF-WEC system reaches 58.05% which breaks the barrier of 50% from linear wave theory for the isolated OB or OWSC devices.

With respect to the inter-comparison of the behavior of the OB and OWSC devices in the MDOF-WEC system, the capture efficiency of the OB in short-period waves is smaller than that of the OWSC, while the opposite trend is found in long-period waves, implying that the OB and OWSC devices are helpful to enhancing wave energy absorption from short waves and long waves, respectively. Because the real irregular wave conditions cover a wide wave period range, this is important for the commercial-scale applications of the practical WEC design. In this regard, the proposed MDOF-WEC system can be more suitable from the full-scale application viewpoint.

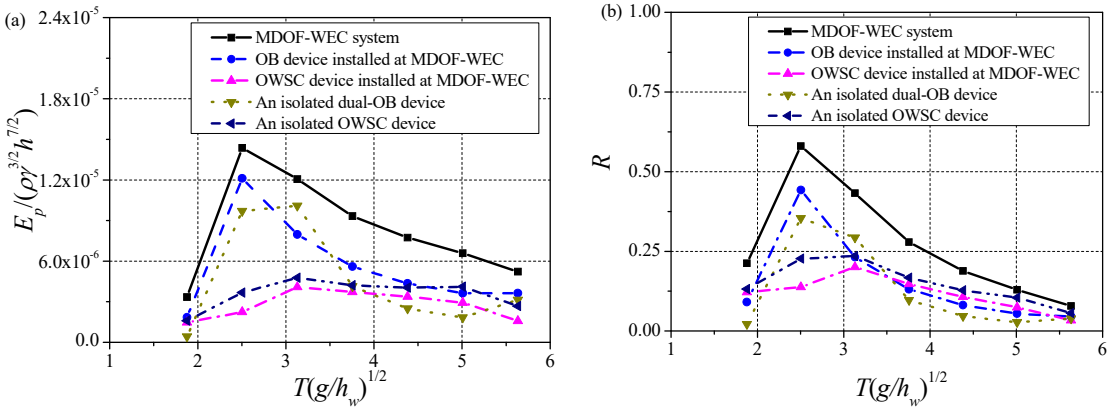

The variation of the wave coefficient C_w recorded by wave gauges WG1 to WG2 against wave period are shown in Fig. 12. The wave coefficient exhibits an oscillation with the incident wave period, and the oscillation amplitude for the MDOF-WEC system is the maximum among three designs. The variation trend of the wave coefficienct at the seaward side is almost identical among three devices, but that at the leeward side for the MDOF-WEC system is more similar to the OWSC device. It is clear that the water surface elevation is significantly reduced by the MDOF-WEC sytem compared with the isolated OB and OWSC devices. This is because the MDOF-WEC is integrated into a semi-submersible platform with six columns, which leads to much stronger interference effect between the WEC device and the platform. In this scenario, the probability of the fatigue damage can be reduced in engineering applications. By comparing Fig. 12 (a) with (b), the wave coefficient at the seaward side is larger than that at the leeward side in short-period waves, but the opposite is true in long waves. This is reasonable because short waves propagate at seaward side and can be partly reflected by the OWSC device, whereas long waves can easily transmit over the OWSC and interact with wave gauge at the downstream form the WEC system. Simiar trends are seen for the time series of water surface elevation at WG1 with wave period $T(g/H_I)^{1/2}$=3.75 and 4.38 as shown in Fig. 13. It can be seen that the signals from the three designs are unsynchronized and thus the water waves arrive their respective peaks at the different instant. Specifically, the water surface for the MDOF-WEC system is in phase with that for the OB device in short waves. The reason is in accordance with the motion comparison shown in Fig. 9, meaning that water surface elevation in short waves includes more radiation waves

generated by the OB motion. However, in long-period waves, the water surface for the MDOF-WEC system is different with that for the OB and OWSC device because of the existence of the platform. Moreover, as the wave period increases, the water surface elevation for the MDOF-WEC device shows stronger nonlinear features compared to that for the isolated OB and OWSC devices. This indicates that the hydrodynamic performance of the MDOF-WEC system in short waves is mainly related to the coupled effect beween the OB and OWSC devices, while that in long waves is affected by the platform.

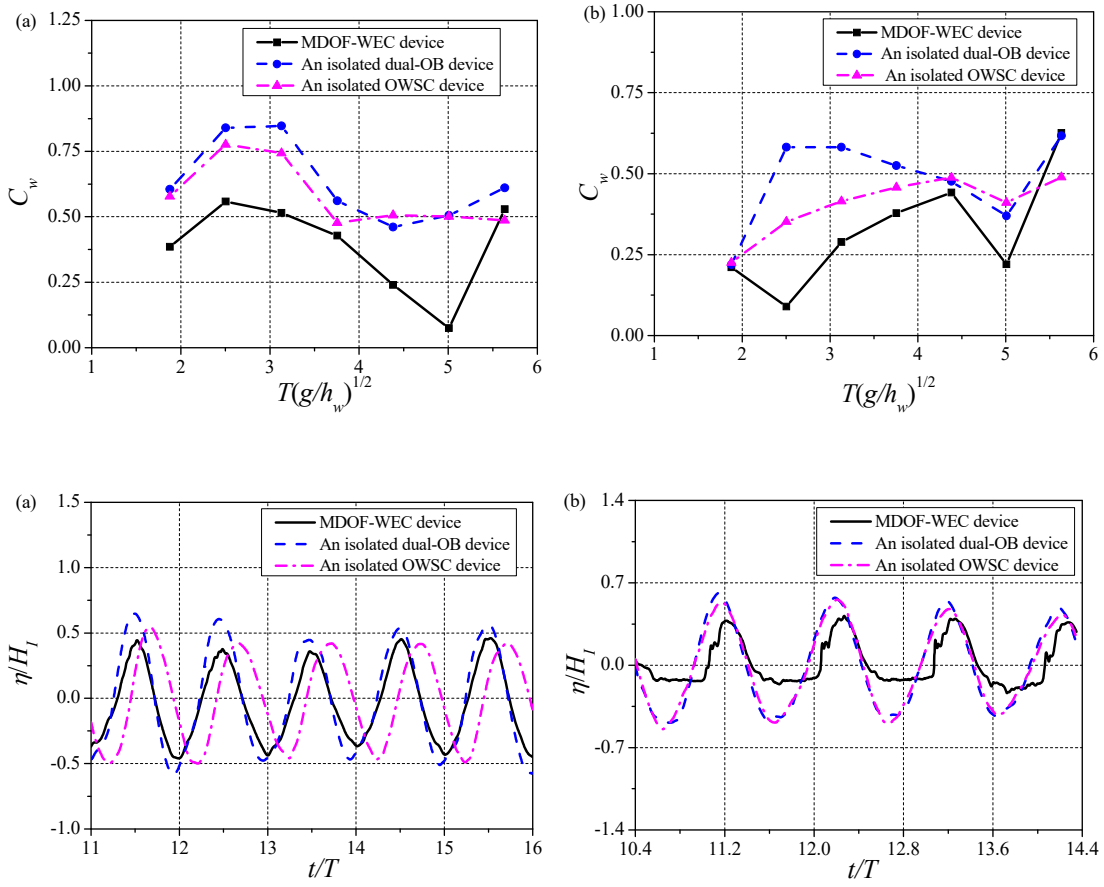

4.2 Effects of incident wave height

The motion RAO and power capture efficiency is desired to be independent of incident wave height for simple single-type WEC devices, and thus can be calculated according to linear wave theory. However, when the present integrated system is subjested to incoming waves with large wave steepness, besides the fundamental wave loads, higher-order waves would be generated due to the complex hydrodynamic coupled effect among OWSC, OB and platform. This requires to analyze the influence degree of nonlinear effects. Fig. 13 displays the surge RAO, the heave RAO, the total translation displacement of each OB and the rotational RAO of the OWSC for the MDOF-WEC system with three different wave heights H_I=0.05 m, 0.10 m and 0.15 m. The other paramters are remained the given values in Section 4.1. It can be observed from Fig. 13(a) and (b) that as the incident wave height increases, the surge curve of the OB device has an oscillating variation with wave period due to the interaction with OWSC, and the heave motion of the OB device increases to certain values then almost keep unchanged in the vicinity of $3<T(g/H_I)^{1/2}<5$.

The total motion displacement of the OB along the body surface of the OWSC slightly increases with the incident wave height as shown in Fig. 13(c), meaning that the more avaialbe wave energy is absorbed by the OB. Fig. 13(d) reveals that the rotational motion of the OWSC device increases with wave height in short-period waves, and suddenly decreases in long-period waves as wave height increases from 0.05 m to 0.10 m. An explanation to such a phenomenon is that the wave nonlinearity becomes more prominent as the wave steepness H_I/λ increases. For stronger nonlinear waves (short-period waves), more higher-order waves are generated due to the interference between platform and WEC devices and are easily reflected by the OWSC, which leads to significant pressure difference beween both sides of the OWSC. Conversely, weaker nonlinear waves (long waves) tansmit over the OWSC and is reflected by the platform, which diminishes the total wave force the due to the phase difference.

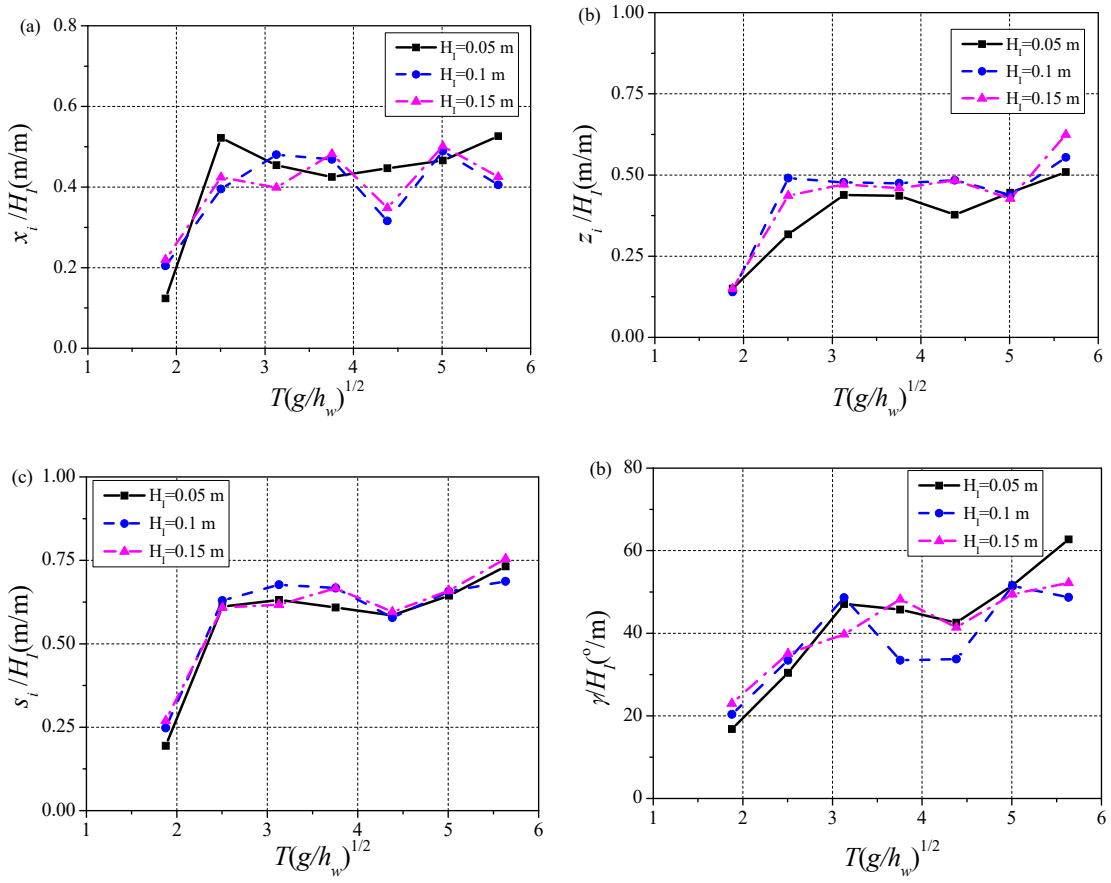

Furthermore, the average generated power by the OB, the OWSC and the integrated sytem is given in Fig. 14 for different wave heights. In order to easier compare the results, all dimensionless average generated power is divided by H_I^2. It can be obtained from Fig. 14 (a) that the average generated power of the OB in the MDOF-WEC system has a slight reduction near the resonant period as wave height increases from 0.05 m to 0.1 m, and then increases with further increasing wave height. There are two peak values in the average generated power of the OWSC in the MDOF-WEC system with increasing wave height. This performance may be caused by the interaction between platform columns and WEC devices and the aforementioned coupled resonant effects of the OB and the OWSC. The larger peak value corresponds to smaller wave period, which is the largest for H_I=0.15 m while the significantly smaller peak value is the largest for H_I=0.1 m. This may be associated with the optimal PTO mechanical coefficiencts repsectively for

the OB and the OWSC. Thus, more detailed discuusions are found in the next sub-section. The variation trend of the total average generated power of the MDOF-WEC system is similar to that of the OB device, indicating that the OB plays a main role in energy extraction compared with the OWSC device.

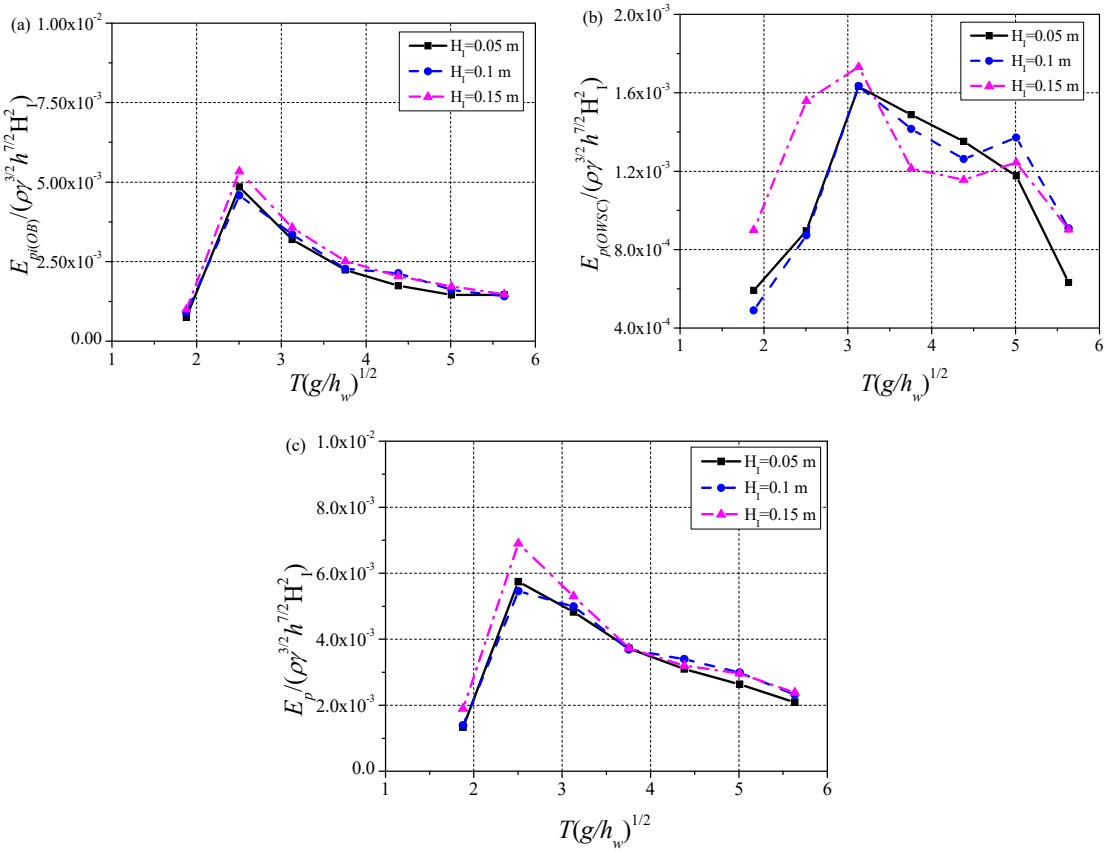

The distribution of the capture efficiency for different wave heights are given in Fig. 15. The capture efficiencies for the total MDOF-WEC and the OB device arrive at the maximum when the wave period $T(g/H_I)^{1/2}$ is equal to 2.5, following the variation trend of the average generated power with wave height. Larger wave height enhances the capture efficiency of the OB device near the resonant wave period. The maximum capture efficiency of the OWSC device moves toward to smaller period with increasing the incident wave height due to the generation of the higher-order waves. Hence, severe waves which can induce more nonlinear waves, can amplify the energy extraction of the MDOF-WEC in the less than resonant period region.

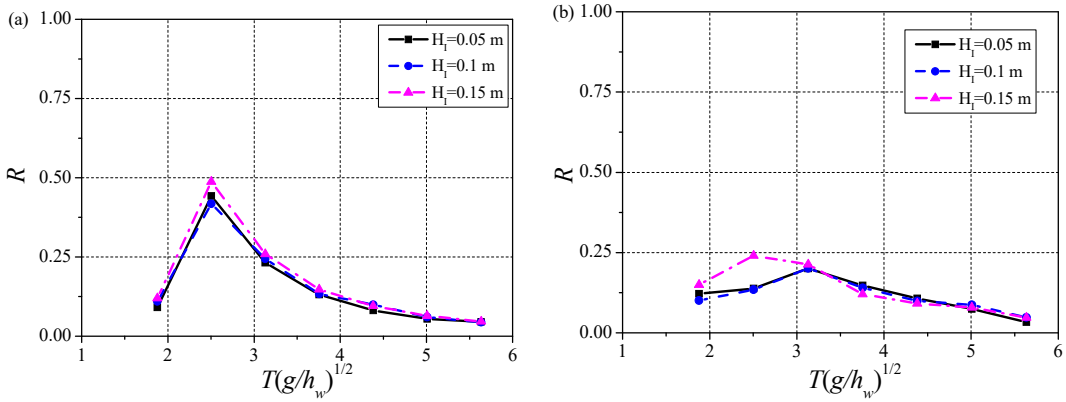

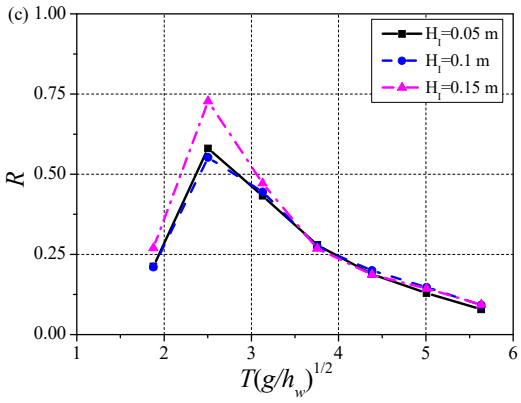

The influence of the wave height on the water surface elevation recorded at the seaward WG1 and the leeward WG2 of the MDOF-WEC system are depicted in Fig. 16 (a) and (b), respectively. As incident wave height increases H_I=0.15 m, the water surface elevation at WG1 is basically unaffected by wave period, but that at WG 2 increases more monotonically with wave period. In general, the influence of incident wave height on the water surface elevation at two measured points is irregular, which is in line with the single-type dual-floater WEC system studied by Zhang [42]. The increased wave nonlinearity would enhance the wave interaction with WEC devices as well as wave energy loss due to stronger vortices developed near the edge of the platform and WEC devices. In addition, there are some phase differences among the water surfaces with different incident wave heights, forming the typical standing wave features. Accordingly, wave nonlinearity is correlated with both wave energy extraction and wave energy dissipation.

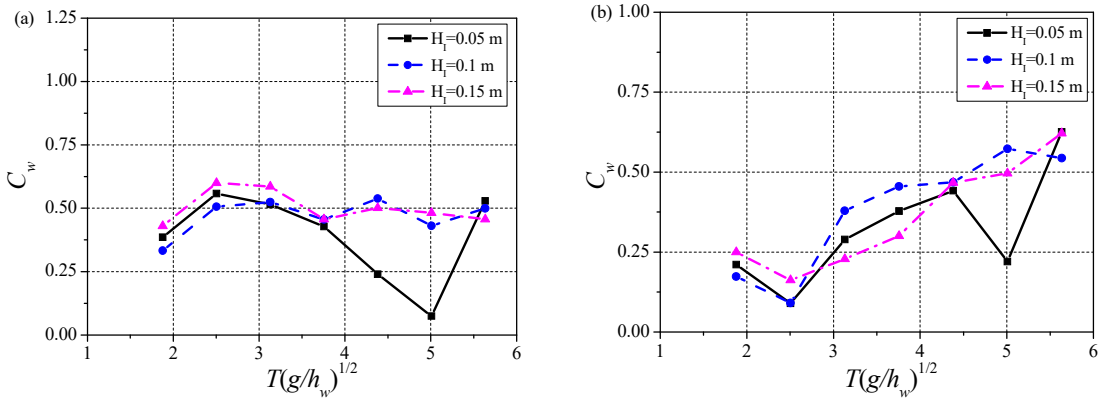

4.3 Optimal PTO damping coefficients

The hybrid-type WEC device comprises two PTO systems: a PTO system corresponding to the OB WECs installed inside OWSC, a PTO system corresponding to the OWSC device hinged to between the OWSC and the platform. Therefore, the optimal PTO sysems are determined in this section, respectively. Firstly, the PTO damping coefficient for the OWSC is fixed as $b_{pto(OWSC)}$=3.5 N•m•s/radian, and a series of different PTO damping coefficients for the OB devices are selected with ranging from $b_{pto(OB)}$=4 N•s/m to 150 N•s/m. Other paramters are kept the same with Section 4.2. Fig. 17 displays the variation of the power capture efficiency for by the OB, the OWSC and the integrated sytem with $b_{pto(OB)}$ for three different incident height. As seen from Fig. 17 (a), the capture efficiency for the OB device increases initially with increasing $b_{pto(OB)}$, and reaches the peak value around $b_{pto(OB)}$=90 N•s/m (H_I=0.05), $b_{pto(OB)}$=60 N•s/m (H_I=0.10) and $b_{pto(OB)}$=40 N•s/m

(H_I=0.15), then decreases after that. This can be predicted by the average generated power indicated in Eq. (17). The wave energy exraction is proportional to both the OB velocity and the PTO damping, while the OB velocity is inversely proportional to the corresponding PTO damping if the incident wave loads are the same. Two limiting cases of capture effieicny R=0 are that $b_{\text{pto(OB)}}$ tends to zero and infinity, which means that incident wave energy is absorbed and then returned to scattering wave energy as the PTO damping increases. Moreover, the optimal PTO damping coefficient for the OB device decreases with increasing incident wave height, demonstrating that Eq. (14) predicted by linear wave theory is only suitable for the cases of small incident wave heights, and the rigous anlysis should conducted when the wave nonlinearity becomes strong. The maximum capture efficiency for the OB device decreases slightly with increasing wave heights, with maximum R=41.69%, 37.85% and 35.79%, respectively. However, the varation of the efficiency curves for the OWSC with $b_{\text{pto(OB)}}$ are largely unchanged by the incident wave height, as shown in Fig. 17 (b). The total capture efficiency for the MDOF-WEC system given in Fig. 17 (c) is controlled by the OB device, showing that the capture efficiency increases with increasing incident wave height in small $b_{\text{pto(OB)}}$ zone, but it is an opposite trend in large $b_{\text{pto(OB)}}$ zone.

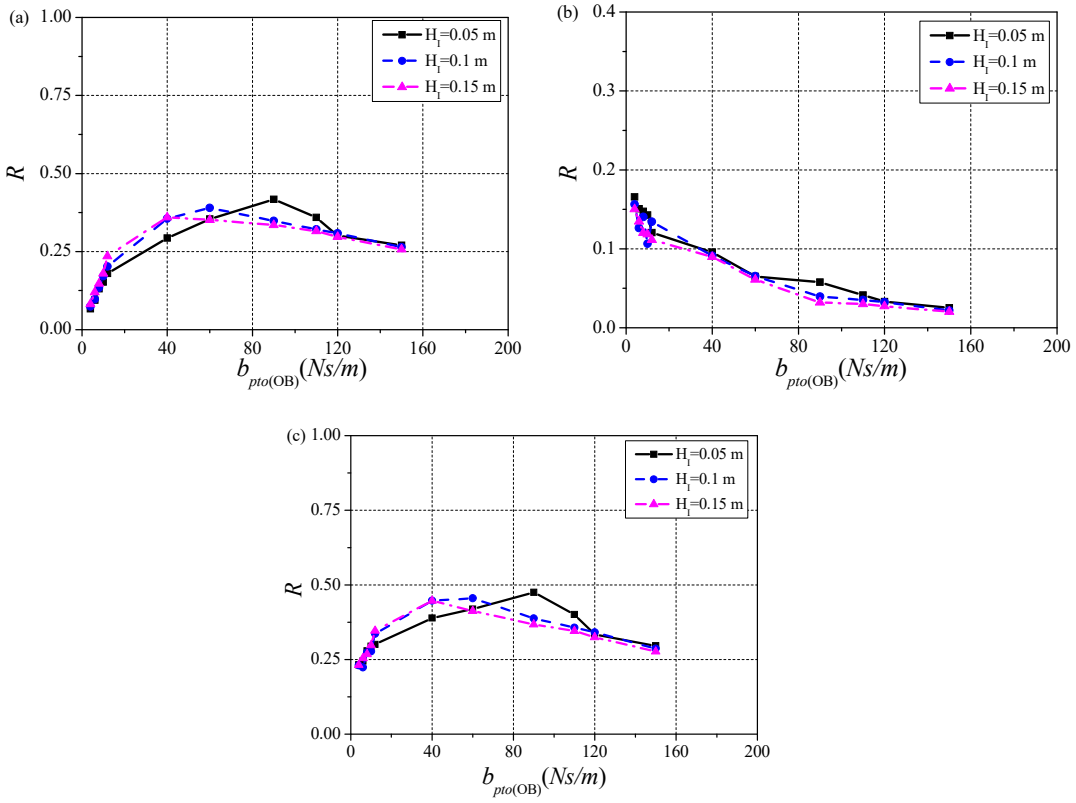

Next, the effects of the PTO damping $b_{\text{pto(OWSC)}}$ for the OWSC on the power capture efficiency of the OB device, the OWSC device and the whole integrated system are given in Fig. 18 (a)-(c), respectively. It can be seen from Fig. 18 (a) that the capture efficiency of the OB device slightly decreases with increasing $b_{\text{pto(OWSC)}}$. This phenomenon may be caused from the reduction of the surge motion of the OB restricted by the OWSC motion. As shown in Fig. 18 (b), the optimal PTO damping of the OWSC device occurs at $b_{\text{pto(OWSC)}}$=10 N•m•s/radian for all incident wave heights, with the maximum efficiency R=24.31% (H_I=0.05 m), R=26.57% (H_I=0.10 m) and R=30.93% (H_I=0.15 m) respectively. This demonstrates that the WEC system designed for a specified range of periods and weak nonlinear waves should also be adequate in the presence of strong nonlinear

waves. For a fixed wave period, the variation of the total efficiency with $b_{pto(OWSC)}$ as shown in Fig. 18 (c) is almost unchanged by the incident wave height.

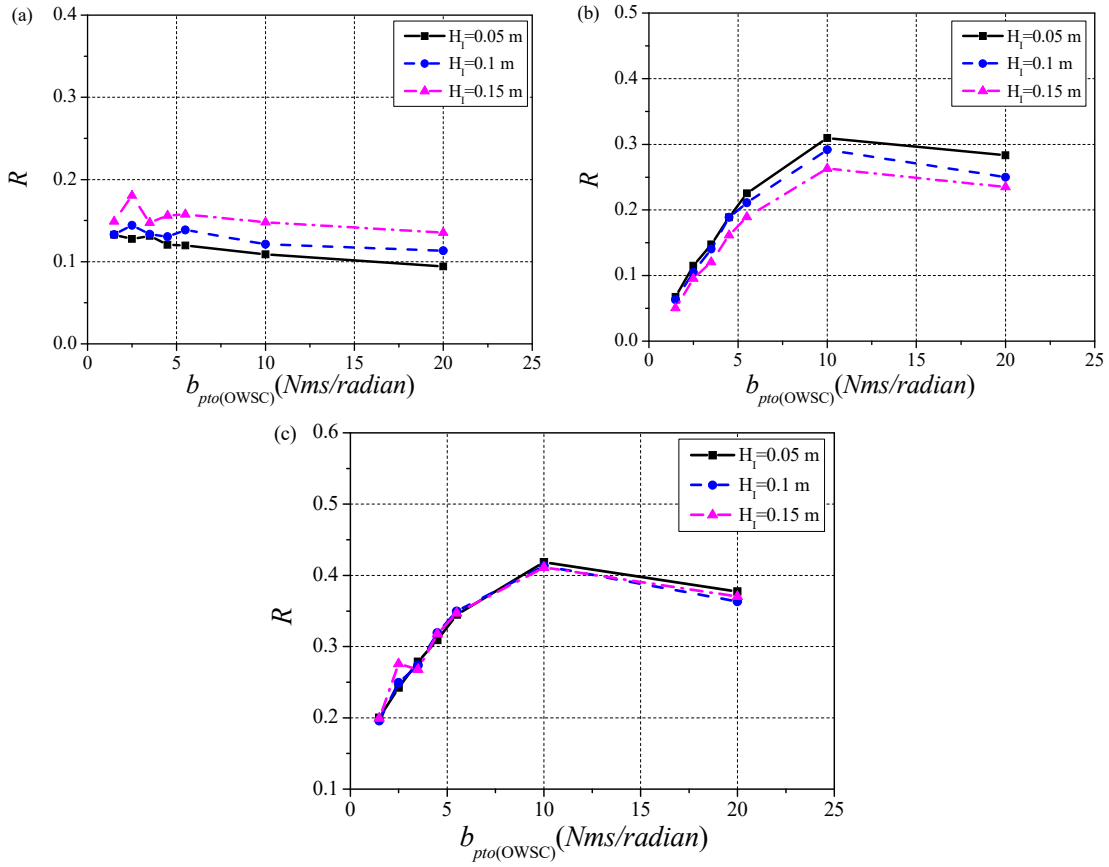

4.4 Effects of OB outer radius

The effects of the outer radius of the OB device on the hydrodynamic performance of the MDOF-WEC system are elaborated in this section. Fig. 19 presents the variation of the motion RAO of the OB device and the OWSC device with three different outer radius, i.e. R_{oo}=0.13 m, 0.14 m and 0.15 m. The incident wave height is set as H_I=0.05 m and other parameters are kept the same with Section 4.2. From Fig. 19 (a), it can be observed that the motion response of the OB device near the resonant period increases with increasing outer radius of the OB, but is basically unchanged at other wave periods. This is not surprising because the wave force on the body bottom increases with increasing the outer radius of the OB in moderate-length waves, while waves are mainly reflected by the OB in short-period waves and move in phase with the OB device in long-period waves. The response oscillation of the OWSC with period becomes more significant with increasing the outer radius of the OB, which is due to the fact that the center of the gravity of the OWSC is closer to the water surface and the corresponding rotational moment arm increases with increasing outer radius of the OB.

Fig. 20 shows the capture efficiency of the OB device, the OWSC device and the whole integrated system with different outer radius of the OB. The variation of the capture efficiency of the OB with the outer radius R_{oo} as shown in Fig. 20 (a) is similar with that of the motion of the OB, while the capture efficiency of the OWSC device as shown in Fig. 20 (b) is insensitive to the outer radius R_{oo} when the inner radius of the OB is kept constant. This is because that the geometric features and the corresponding PTO coefficient of the OWSC are not changed with the increasing outer radius R_{oo}. The occurring period of the maximum efficiency is almost

independent on the outer radius R_{oo}. The overall capture efficiency as shown in Fig. 20 (c) is simultaneously controlled by the hybrid-type WEC devices, and its maximum value is related to the coupled resonant effect between the OB and OWSC devices.

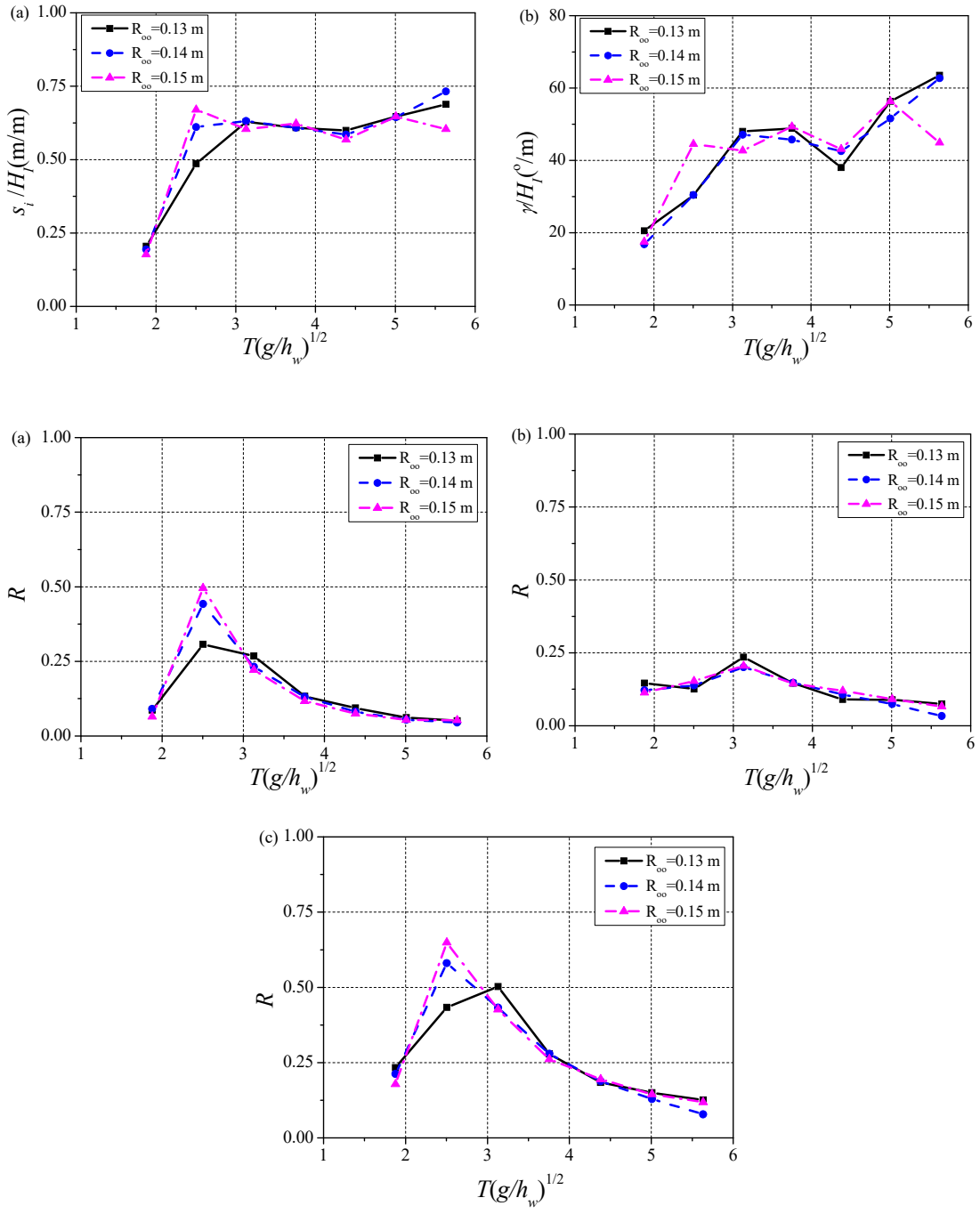

5. Conclusions

In this study, a novel multi-purpose platform including the advantages and design features of a moonpool-type floating breakwater and an array of heaving OB WECs is proposed, and the corresponding hydrodynamics is investigated using a developed 3D time-domain NWT. The wave attenuation capacity, the wave energy extraction, and the mutual relationship between the breakwater and the WECs are emphatically discussed, respectively. The following conclusions can

be obtained from this investigation:

(1) The introduction of the moonpools can increase significantly the heaving response and wave energy extraction of WECs in the long wave region compared to the isolated WEC layouts. This is due to the long waves being transmitted to the moonpools more easily to cause the internal fluid motion. Moreover, due to the wave absorption of the WECs, the wave attenuation capacity of the multi-purpose floating platform has certain enhancement compared to the single breakwater.

(2) In the multi-purpose floating platform, the WECs with larger diameter can capture more wave energy, while the transmission coefficient is not very sensitive to the horizontal dimension of the WEC in the short wave region. The interaction factors with different WEC diameters implies that the wave energy extraction of the WEC is not only improved by the moonpool between two pontoons but also has a positive effect on the total wave attenuation.

(3) Stronger wave nonlinearity reduces the motion responses, the average generated power, the capture efficiency, and the transmission coefficient of the multi-purpose platform, and leads to a smaller optimal PTO damping corresponding to maximum energy extraction. The increase of PTO damping cannot affect the reflection coefficient but can reduce the transmission at a large wave amplitude.

(4) Thinner moonpools play a more dominant role in wave energy conversion than fatter moonpools for an unequal layout of moonpools, especially in the short wave region because the internal fluid resonance in the moonpool becomes stronger. By adjusting the moonpool length and the moonpool number in a multi-purpose platform, the whole floating system can broaden the effective bandwidth for a practical wave farm.

(5) Oblique waves amplify wave energy extraction of the multi-purpose platform in the short wave region due to a more violent mass exchange of fluid from the moonpool to the outer domain. In addition, the wave attenuation capacity in oblique waves can be improved as a result of reduced effective wavelength in the normal direction of the platform length.

The novel conceptual design of the multi-purpose platform system can provide a promising way to achieve the synergies between offshore infrastructural protection and wave energy utilization, helping to guide geometric configuration design and commercial operation as soon as possible. The developed nonlinear time-domain model can be used as an accurate numerical tool for parametric optimization, durability analysis, and comparison with tested data. Future studies will focus on extending the model to simulate irregular wave conditions which may have seasonal physical characteristics.

CRediT authorship contribution statement

Yong Cheng: Methodology, Software, Data curation, Writing-original draft, Supervision. **Chen Xi:** Validation, Formal analysis, Writing-original draft, Investigation. **Saishuai Dai:** Formal analysis, Data curation, Writing-review & editing, Supervision. **Chunyan Ji:** Writing-review & editing, Supervision, administration. **Margot Cocard:** Formal analysis, Data curation, Writing-review & editing. **Zhiming Yuan:** Writing-review &editing. **Atilla Incecik:** Supervision.

Declaration of Competing Interest

The authors declare that they have no known competing financial interests or personal relationships that could have appeared to influence the work reported in this paper.

Acknowledgment

The authors are grateful to the National Natural Science Foundation of China (Grant No. 52025112, 51861130358, 51609109), the State Key Laboratory of Ocean Engineering, China (Shanghai Jiao Tong University) (Grant No. 1905) and the Newton Advanced Fellowships (Grant No. NAF\R1\180304) by the Royal Society for supporting this work.

References

[1] Edenhofer O, Pichs-Madruga R, Sokona Y, Seyboth K, Kadner S, Zwickel T, et al. Renewable energy sources and climate change mitigation: special report of the intergovernmental panel on climate change. Cambridge University Press; 2011.

[2] Sheng W. Wave energy conversion and hydrodynamics modelling technologies: a review. Renew Sustain Energy Rev 2019;109:482–498.

[3] Lopez I, Andreu J, Ceballos S, Martínez De Alegría I, Kortabarria I. Review of wave energy technologies and the necessary power-equipment. Renew Sustain Energy Rev 2013;27:413–434.

[4] Falnes J.. A review of wave-energy extraction. Mar Struct 2007;20:185–201.

[5] Salter SH. Wave power. Nature 1974,249:720–724.

[6] Whittaker T, Folley M. Nearshore oscillating wave surge converters and the development of Oyster. Phil Trans R Soc A 2012;370:345e64.

[7] Dalton GJ，Alcorn R，Lewis T. Case study feasibility analysis of the pelamis wave energy convertor in Ireland，portugal and north america. Renew Energy. 2010;35(2):443-455.

[8] Folley M, Whittaker TJT, Van't Hoff J. The design of small seabed-mounted bottom hinged wave energy converters. In: Proceedings of the seventh European wave and tidal energy conference; 2007.

[9] Cleason L, Forsberg J, Rylander A. Contribution to the theory and experience of energy production and transmission from the buoy-concept. In：Proceedings of 2nd International Symposium on Wave Energy Utilization, 1982：345-370.

[10] Falcão AFDO. Wave energy utilization: a review of the technologies, Renew Sustain Energy Rev. 2010;14 (3): 899-918.

[11] Kim SJ, Koo W, Min EH, Jang H, Youn D, Lee B. Experimental study on hydrodynamic performance and wave power takeoff for heaving wave energy converter. J Ocean Eng Technol 2016;30:361–366.

[12] Kong F, Su W, Liu H, Collu M, Lin Z, Chen H, Zheng X. Investigation on PTO control of a Combined Axisymmetric Buoy-WEC(CAB-WEC), Ocean Eng 2019,188:106245.

[13] Guo W, Zhou YH, Zhang WC, Zhao QS. Hydrodynamic analysis and power conversion for point Absorber WEC with two degrees of freedom using CFD. China Ocean Eng 2018;38(6):718–729.

[14] Bailey H, Robertson B, Buckham B. Variability and stochastic simulation of power from wave energy converter arrays. Renew Energy 2018;115:721-733.

[15] Harris RE, Johanning L, Wolfram J. Mooring systems for wave energy converters: A review of design issues and choices. 3rd Int Conf Mar Renew Energy 2004:1–10.

[16] Asai T, Sugiura K. Numerical evaluation of a two-body point absorber wave energy converter with a tuned inerter. Renew Energy 2021;171:217-226.

[17] Folley M, Whittaker TJT. Analysis of the nearshore wave energy resource. Renew Energy 2009;34:1709-1715.

[18] Folley M, Whittaker TJT, Henry A. The performance of a wave energy converter in shallow water. Sixth European Wave and Tidal Energy Conference, Glasgow, 2005.

[19] Folley M, Whittaker TJT, Henry A. The effect of water depth on the performance of a small surging wave energy conver. Ocean Eng 2007;34:1265-1274.

[20] Cheng Y, Li G, Ji CY, Zhai GJ. Solitary wave slamming on an Oscillating Wave Surge Converter over varying

topography in the presence of collinear currents. Phys Fluids 2020; 32: 047102.

[21] Pereiras B, López I, Castro F, Iglesias G. Non-dimensional analysis for matching an impulse turbine to an OWC(oscillating water column) with an optimum energy transfer. Energy 2015;87:481-489.

[22] Zheng S, Antonini A, Zhang Y, Greaves D, Miles J, Iglesias G. Wave power extraction from multiple oscillating water columns along a straight coast. J Fluid Mech 2019;878:445-480.

[23] Heo S, Koo W. Numerical procedures for dynamic response and reaction force analysis of a heaving-point absorber wave energy converter, Ocean Eng, 2020;200:107070.

[24] Michailides C, Angelides DC. Modeling of energy extraction and behavior of a flexible floating breakwater. Appl Ocean Res 2012;35:77–94.

[25] He F, Huang Z. Hydrodynamic performance of pile-supported OWC-type structures as breakwaters: An experimental study. Ocean Eng 2014;88:618–626.

[26] Liu X, Liu Y, Lin P, Li A. Numerical simulation of wave overtopping above perforated caisson breakwaters. Coast Eng 2021;163:103795.

[27] Zhang HM, Zhou BZ, Vogel C, Willden R, Zang J, Zhang L. Hydrodynamic performance of a floating breakwater as an oscillating-buoy type wave energy converter. Appl Energy 2020;257:113996.

[28] Liu HF, Bi CW, Zhao YP. Experimental and numerical study of the hydrodynamic characteristics of a semisubmersible aquaculture facility in waves. Ocean Eng 2020;214:107714.

[29] Muliawan MJ, Karimirad M, Moan T. Dynamic response and power performance of a combined Spar-type floating wind turbine and coaxial floating wave energy converter. Renew Energy 2013;50:47-57.

[30] Ren NX, Ma Z, Fan TH, Zhai GJ, Ou JP. Experimental and numerical study of hydrodynamic responses of a new combined monopole wind turbine and a heave-type wave energy converter under typical operational conditions. Ocean Eng 2018;159:1-8.

[31] Hu JJ, Zhou BZ, Vogel C, Liu P, Willden R, Sun K, et al. Optimal design and performance analysis of a hybrid system combing a floating wind platform and wave energy converters. Appl Energy 2020; 269: 114998.

[32] Fiaschi D, Manfrida G, Secchi R, Tempesti D. A versatile system for offshore energy conversion including diversified storage. Energy 2012;48:566–576.

[33] Zhang HC, Xu DL, Ding R, Zhao H, Lu Y, Wu YS. Embedded power take-off in hinged modularized floating platform for wave energy harvesting and pitch motion suppression. Renew Energy 2019;138:1176-1188.

[34] Sricharan VVS, Chandrasekaran S. Time-domain analysis of a bean-shaped multi-body floating wave energy converter with a hydraulic power take-off using WEC-Sim. Energy 2021;223:119985.

[35] Zhao X, Zhang Y, Li M, Johanning L. Hydrodynamic performance of a Comb-Type Breakwater-WEC system: An analytical study. Renew Energy 2020;159:33-49.

[36] Sun P, Hu S, He H, Zheng S, Chen H, Yang S, Ji Z. Structural optimization on the oscillating-array-buoys for energy-capturing enhancement of a novel floating wave energy converter system. Energy Convers Manage 2021;228:113693.

[37] Ren NX, Ma Z, Shan BH, Ning DZ, Ou JP. Experimental and numerical study of dynamic responses of a new combined TLP type floating wind turbine and a wave energy converter under operational conditions. Renew Energy 2020;151:966-974.

[38] Zhong Q, Yeung RW. Wave-body interactions among energy absorbers in a wave farm. Appl Energy 2019;233:1051-1064.

[39] Zheng S, Zhang Y, Iglesias G. Power capture performance of hybrid wave farms combining different wave energy conversion technologies: The H-factor. Energy 2020;204:117920.

[40] Zhou Y, Ning D, Shi W, Johanning L, Liang D. Hydrodynamic investigation on an OWC wave energy

converter integrated into an offshore wind turbine monopole. Coast Eng 2020;162:103731.

[41] Reabroy R, Zheng XB, Zhang L, Zang J, Yuan Z, Liu M, Sun K, Tiaple Y. Hydrodynamic response and power efficiency analysis of heaving wave energy converter integrated with breakwater. Energy Convers Manage 2019;195:1174-1186.

[42] Zhang HM, Zhou BZ, Vogel C, Willden R, Zang J, Geng J. Hydrodynamic performance of a dual-floater hybrid system combining a floating breakwater and an oscillating-buoy type wave energy converter. Appl Energy 2020;259:114212.

[43] Windt C, Davidson J, Ransley EJ, Greaves D, Jakobsen M, Kramer M, Ringwood JV. Validation of a CFD-based numerical wave tank model for the power production assessment of the wavestar ocean wave energy converter. Renew Energy 2020;146:2499-2516.

[44] Marchesi E, Negri M, Malavasi S. Development and analysis of a numerical model for a two-oscillating-body wave energy converter in shallow water. Ocean Eng 2020;214:107765.